Sun et al. *NPG Asia Materials* (2023)15:6
https://doi.org/10.1038/s41427-022-00458-5

NPG Asia Materials

ARTICLE Open Access

2D carbon network arranged into high-order 3D nanotube arrays on a flexible microelectrode: integration into electrochemical microbiosensor devices for cancer detection

Yimin Sun[1], Xulin Dong[2], Hu He[3], Yan Zhang[2], Kai Chi[2], Yun Xu[2], Muhammad Asif[1], Xuan Yang[2], Wenshan He[4], Kin Liao[5] and Fei Xiao[2]

Abstract

In this work, we develop a new type of mesoporous 2D N, B, and P codoped carbon network (NBP-CNW) arranged into high-order 3D nanotube arrays (NTAs), which are wrapped onto a flexible carbon fiber microelectrode, and this microelectrode is employed as a high-performance carbon-based nanocatalyst for electrochemical biosensing. The NBP-CNW-NTAs synthesized by a facile, controllable, ecofriendly and sustainable template strategy using ionic liquids as precursors possess a high structural stability, large surface area, abundant active sites, and effective charge transport pathways, which dramatically improve their electrocatalytic activity and durability in the redox reaction of cancer biomarker H_2O_2. Benefiting from these unique structural merits, superb electrochemical activity and good biocompatibility, the NBP-CNW-NTAs-modified microelectrode demonstrates excellent sensing performance toward H_2O_2 and is embedded in a homemade microfluidic electrochemical biosensor chip for the real-time tracking of H_2O_2 secreted from different live cancer cells with or without radiotherapy treatment, which provides a new strategy for distinguishing the types of cancer cells and evaluating the radiotherapeutic efficacy of cancer cells. Furthermore, the functional microelectrode is integrated into an implantable probe for the in situ detection of surgically resected human specimens to distinguish cancer tissues from normal tissues. These will be of vital significance for cancer diagnoses and therapy in clinical practice.

Introduction

Recent nanotechnological progress in structural/functional materials has stimulated tremendous research interest in the development of various carbon allotropes, including graphene quantum dots and nanodiamonds[1], 1D carbon nanotubes and nanohorns[2], and 2D monolayer/multilayer graphene and amorphous/graphitic/diamond-like carbon networks[3], due to their intrinsic physicochemical properties, extraordinary mechanical strength and unique physiological and pharmacological effects that are highly desirable for diverse applications in catalysis, energy-related systems, biosensing and biomedical engineering[4–6]. More importantly, these low-dimensional nanocarbon materials can be self-assembled or coassembled into various 3D macroscopic architectures[7–9], which opens new avenues for their promising application as high-performance electrode materials in next-generation flexible/stretchable batteries, implantable and wearable (micro)electronic devices and artificially intelligent sensors[10–15]. Nevertheless, low-dimensional nanocarbon materials are easily restacked with each other or

Correspondence: Wenshan He (hewenshan@hust.edu.cn) or Kin Liao (kin.liao@ku.ac.ae) or Fei Xiao (xiaofei@hust.edu.cn)
[1]Hubei Key Laboratory of Plasma Chemistry and Advanced Materials, School of Materials Science and Engineering, Wuhan Institute of Technology, Wuhan 430073, P. R. China
[2]Key Laboratory of Material Chemistry for Energy Conversion and Storage, School of Chemistry and Chemical Engineering, Huazhong University of Science & Technology, Wuhan 430074, P. R. China
Full list of author information is available at the end of the article

aggregated during the assembly process, which seriously decreases their effective active surface area and structural stability[16]. As a result, strategies for arranging nanocarbon materials to form higher-order architectures by template methods are quite desirable because they are highly controllable and can effectively avoid the restacking and aggregation of carbon building blocks[17]. For the synthesis of nanocarbon materials with higher-order architectures by well-developed template methods, several carbon precursors, such as glucose[18], polydopamine[19], and other heteroatom polymers[20], have been utilized. These precursors can not only be easily coated on various template surfaces but also result in high carbonization yields. However, it is still a challenge to use these precursors for the synthesis of carbon-based nanomaterials with desirable features, including controllable nano/mesostructures, superb chemical/electronic properties, multifunctionality, and so on.

In this work, we develop a facile, controllable, ecofriendly and sustainable strategy for synthesizing a novel high-order 3D nanotube arrays (NTAs) arranged from a mesoporous 2D multiheteroatom codoped carbon network (CNW) by the direct carbonization of a new class of ionic liquids (ILs). In recent studies, ILs that generally consist of adjustable organic cations and anions have emerged as promising green precursors for synthesizing heteroatom-doped carbon materials. ILs have several important merits, including their charge nature induced negligible vapor pressure during the high-temperature heating process, "universal" surface activity for coating almost all surfaces to form carbon nanomaterials with different morphologies[21,22], and tunable chemical structures through incorporating multiple heteroatom-doped carbon species with conjugated N, S and B atoms by smartly selecting the anions and cations of ILs[23]. Herein, N, B, and P codoped CNW (NBP-CNW)-NTAs were derived from task-specific ILs, i.e., 1-vinyl-3-ethyl imidazole tetrafluoroborate ([VEIM]BF_4) and 1-octyl-3-methyl imidazole hexafluorophosphate ([OMIM]PF_6), using a 3D high-order ZnO-nanorod arrays (NRAs) grown on activated carbon fiber (CFs) as the sacrificial template. We found that the [VEIM]BF_4 monomer containing a hydrophilic anionic group and a cross-linkable cationic group wrapped the ZnO-NRAs substrate and self-polymerized, which further carbonized into a N and B codoped carbon layer under the high-temperature heating process. During this process, noncarbonizable [OMIM]PF_6 molecules underwent thermal decomposition, which simultaneously functioned as the pore-forming agent as well as N and P sources to produce many mesopores and introduce an abundance of heteroatoms in the carbon layer. After removing the ZnO-NRAs template, high-order 3D NBP-CNW-NTAs wrapped on CFs were obtained. By using this method, different carbon nanomaterials with 3D high-order architectures, desirable nano/mesostructures, tunable porosity, and changeable doped heteroatoms can be achieved by adjusting the sacrificial template structure and the molecular organization of the anions and cations of the ILs.

The practical application of the resultant NBP-CNW-NTAs-modified CF (NBP-CNW-NTAs/CF) microelectrode was explored in the electrochemical sensing of the biomarker H_2O_2 secreted from different cancer cells and tissues. H_2O_2 is a major reactive oxygen species in unicellular and multicellular organisms[24], and its level in various human samples is of great significance for cancer diagnosis and assessment[25]. Our results demonstrated that the NBP-CNW-NTAs/CFs microelectrode benefitted from the hierarchically porous architecture achieved by the formation of macropores in the 3D high-order NTAs within the numerous mesopores in 2D CNWs and therefore exhibited a large electrochemically active surface area (ECSA), abundant surface active sites, effective charge transport pathways, and a high structural stability, which dramatically enhanced its electrocatalytic reactivity and durability to H_2O_2. Furthermore, homogeneous heteroatom (i.e., N, B and P) doping was accomplished fairly easily and consequently changed the charge density and electron cloud arrangement of carbon atoms[26], thus enhancing the electronic conductivity and wettability of carbon species.

Benefiting from its unique structural merits and high reactivity, the hierarchically structured NBP-CNW-NTAs/CF microelectrode exhibited good electrochemical sensing performance toward H_2O_2, which included a low detection limit of 500 nM (a signal-to-noise ratio of $S/N = 3$), a wide linear dynamic range up to 15.92 mM, a high sensitivity of 61.8 $\mu A\ cm^{-2}\ mM^{-1}$, high anti-interference ability, good mechanical and long-term stability, and excellent biocompatibility, which enabled it to be embedded in a microfluidic chip for the real-time tracking of H_2O_2 secreted from different live cancer cell lines (i.e., breast cancer cells, hepatoma cells and cervical cancer cells) with or without radiotherapy treatment, which provides a new strategy for distinguishing the types of cancer cells and evaluating radiotherapeutic efficacy toward different cells. Furthermore, the proposed nanostructured microelectrode was also integrated into an implantable probe for the in situ minimally invasive detection of surgically resected human breast specimens to distinguish tumor tissues from normal tissues. Accordingly, we fabricated novel electrochemical microbiosensors based on the NBP-CNW-NTAs/CF microelectrode for the sensitive and real detection of cancer cells and tissues, which will be of vital significance for cancer diagnosis and management in clinical practice.

Material and methods

Preparation of hierarchical structured microelectrode

The preparation process of the nanostructured microelectrode is shown in Fig. 1A. The carbon fibers (CFs) were activated by being immersed in H_2O_2 (30%) at 60 °C

for 24 h, washed with deionized water three times and dried at 60 °C. ZnO-NRAs were grown on the CFs by an electrodeposition process according to our previous work[18], as described in the Supporting Information. For the preparation of the NBP-CNW-NTAs/CF, two types of ILs, i.e., [VEIM]BF_4 and [OMIM]PF_6 (volume ratio 4:1), were mixed and stirred to generate a homogeneous liquid that was then coated on the surface of the ZnO-NRAs. Then, the ILs coated ZnO-NRAs were heated at 750 °C in a quartz tube under an Ar atmosphere at a heating rate of 2 °C min^{-1} for 3 h to transform the IL layer into a multiheteroatom codoped porous carbon layer. To remove the ZnO-NRAs template, the product was immersed in 0.1 M HCl solution for 6 h. After being washed with deionized water and dried at 80 °C, NBP-CNW-NTAs/CF were obtained. Furthermore, the [VEIM]BF_4 monomer was heated from room temperature to 300 °C at a rate of 2 °C min^{-1} and then cooled naturally in the furnace tube under an Ar atmosphere to synthesize P[VEIM]BF_4 by a thermal-initiation free-radical polymerization method.

Fabrication of an electrochemical microfluidic chip and implantable chip

A microfluidic chip was elaborately designed using AutoCAD 2008 software (Autodesk, U.S.A.) and fabricated by Mesobiosystem Co., Ltd. (Wuhan, China); the details are described in the Supporting Information. The NBP-CNW-NTAs/CF microelectrode, Pt wire (50 μm) and Ag/AgCl electrode (obtained by depositing a AgCl layer on Ag wire, 50 μm) were placed in the detection chamber and functioned as the working electrode (WE), counter electrode (CE) and reference electrode (RE), respectively. For electrochemical testing, 10 μL of human cell sample was pumped into the chip through the inlet channel and gathered in the detection chamber. For the construction of an implantable probe, a NBP-CNW-NTAs/CF microelectrode, Pt wire and Ag/AgCl electrode were integrated into a homemade probe, which was carefully inserted into human tissues for minimally invasive detection. The three-electrode system was connected to a portable bipotentiostat for electrochemical testing.

Cell culture and tissues

Hepatoma cells (HepG2), cervical cancer cells (HeLa) and breast cancer cells (MCF-7) were obtained from Union Hospital, Tongji Medical College, Huazhong University of Science & Technology (Wuhan, China). All cells were cultured in Dulbecco's modified Eagle's medium (DMEM) with 10% fetal bovine serum (FBS) and 1% penicillin–streptomycin in a humidified cell incubator at 37 °C containing 5% CO_2. After growing to ~90% confluence, the cells were washed and collected by centrifugation for testing. The number of live cells was determined by the cell counter method. The cytotoxicity of the NBP-CNW-NTAs/CF microelectrode was evaluated by a standard cell counting Kit-8 (CCK-8) assay. Surgically resected clinical specimens of human primary breast tumors (tumor tissue I and II) were also received from Union Hospital. A control sample was obtained from the enclosed adipose tissue of the cancer tissue. All the specimens were washed with PBS solution several times and soaked in PBS solution at 37 °C for electrochemical testing.

Results and discussion

Morphological and compositional characterization

The morphologies of different samples were first investigated with scanning electron microscopy (SEM) images. As shown in Fig. 1B, the flexible CF exhibited a typical diameter of approximately 10 μm and a relatively rough surface after being activated. The large number of functional groups on the surface of the activated CF acted as active sites for the nucleation and growth of the ZnO-NRAs. Figure 1C–E show that close-packed ZnO nanorods, which are hexagonal prisms with smooth crystal surfaces, were entirely wrapped on the CFs by electrodeposition. NBP-CNW-NTAs were obtained by coating the ZnO-NRAs with an IL mixture of [VEIM]BF_4 and [OMIM]PF_6 and then heating at a low rate. During this process, a thermal-initiated free-radical polymerization of [VEIM]BF_4 first occurred at a relatively low temperature (i.e., 300 °C), where the carbon atoms in the vinyl groups became sp^3 hybridized during thermal polymerization under carbonization conditions[27]. The number average molecular weights (Mn) and polydispersity index (PDI) of the product evaluated by gel permeation chromatography (GPC) were 4.74 kDa and 1.012, respectively (Fig. S1), which authenticates the successful polymerization of [VEIM]BF_4 into P[VEIM]BF_4 at 300 °C. The as-obtained P[VEIM]BF_4 adhered onto the ZnO nanorods to form a compact layer. With the elevation of the heating temperature, P[VEIM]BF_4 began to transform into N and B codoped carbon with a minimal loss of reactant during carbonization[28]. Moreover, [OMIM]PF_6 monomers underwent thermal decomposition, and N and P atoms from [OMIM]PF_6 were doped into carbon to form N, B and P codoped carbon species. After removing the ZnO-NRAs template, 3D high-order NBP-CNW-NTAs that inherited the structure of the ZnO-NRAs were formed on the CFs (Fig. 1F–H). The high-magnification SEM image reveals that the as-obtained NBP-CNW-NTAs exhibited a typical loofah-like morphology and were rich in interconnected pores (Fig. 1I) because [OMIM]PF_6 functioned as a pore-forming agent during its thermal decomposition in the carbonization process and resulted in the formation of a large number of pores in the carbon layer[22]. Figure 1J–L show the transmission electron microscopy (TEM) images of the 2D CNW fragment exfoliated from the CF

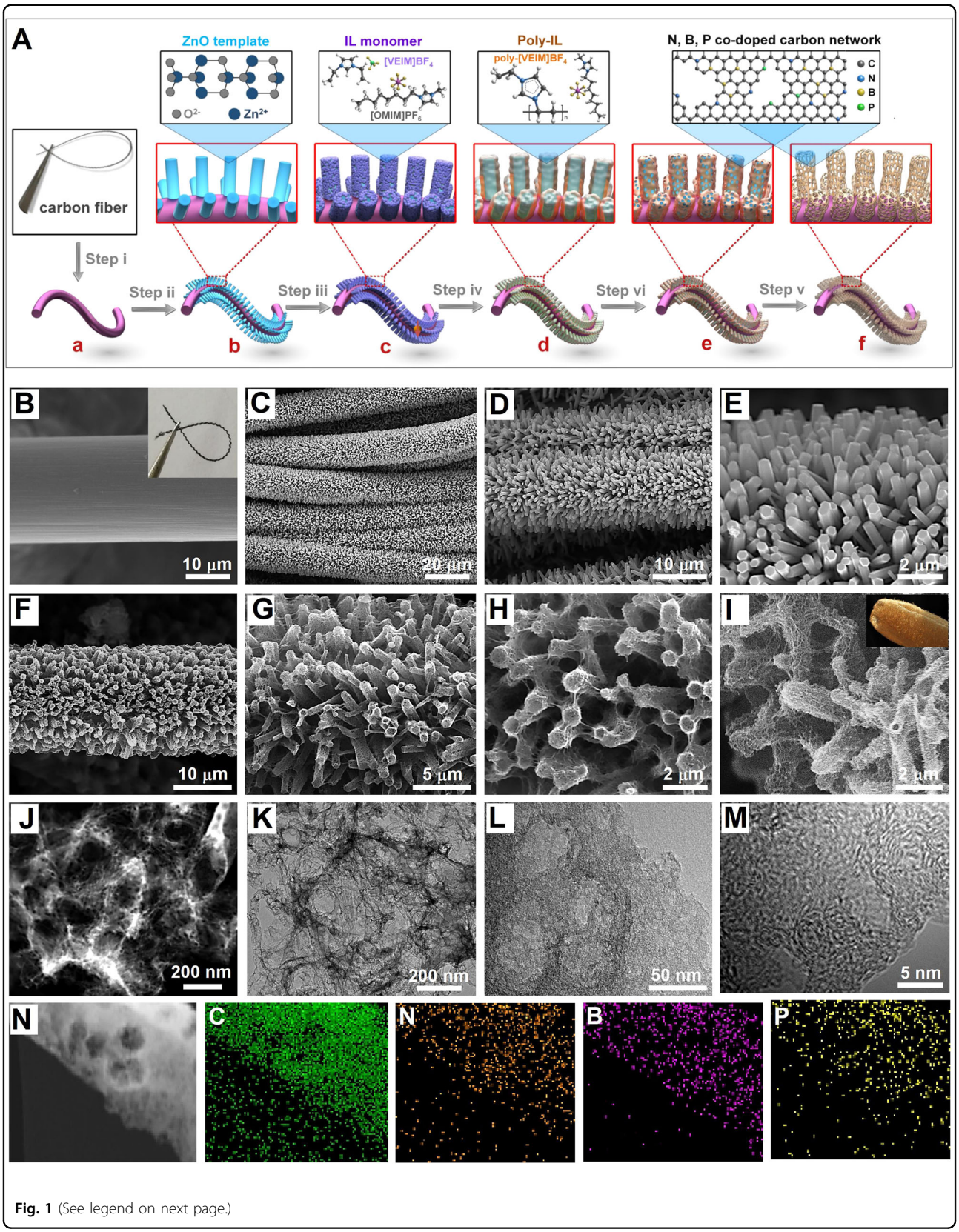

Fig. 1 (See legend on next page.)

(see figure on previous page)

Fig. 1 The synthesis process and morphological feature of NBP-CNW-NTAs/CF and its precursors. A Schematic illustration of the fabrication procedure of the hierarchical structured hybrid microelectrode: (a) activated CF, (b) ZnO-NRAs/CF, (c) ZnO-NRAs@[VEIM]BF_4-[OMIM]PF_6/CF, (d) ZnO-NRAs@P[VEIM]BF_4-[OMIM]PF_6/CF, (e) ZnO-NRAs@NBP-CNW/CF, and (f) NBP-CNW-NTAs/CF. Step i: Activating CF by immersion in H_2O_2; Step ii: Growth of ZnO-NRAs on CF via electrodeposition; Step iii: Dip-coating IL mixture of [VEIM]BF_4-[OMIM]PF_6 on ZnO-NRAs; Step iv: Thermal-initiation free-radical polymerization of [VEIM]BF_4 monomer to form P[VEIM]BF_4 layer on ZnO-NRAs by heating from room temperature to 300 °C; Step v- Carbonization of P[VEIM]BF_4-[OMIM]PF_6 layer into NBP-CNW by heating to 750 °C; Step vi: Removing ZnO-NRAs template to form NBP-CNW-NTAs. SEM images of (**B**) activated CF; inset is the digital photograph of CF. SEM images of (**C**–**E**) ZnO-NRAs/CF and (**F**–**I**) NBP-CNW-NTAs/CF at different magnifications. **J** Dark-field and (**K**–**M**) bright-field TEM images of NBP-CNW at different magnifications. **N** Scanning elemental mapping of NBP-CNW.

substrate, indicating a typical cross-linked porous structure. From the high-resolution TEM image, it can be observed that the carbon species exhibited a partially graphitic structure (Fig. 1M). The TEM mapping of the as-obtained CNWs shown in Fig. 1N demonstrated the homogeneous dispersion of C, N, B and P, confirming the successful synthesis of multiple heteroatom-doped CNW materials.

To reveal the formation mechanism of the proposed NBP-CNW-NTAs, the effects of the IL precursors on the morphology and structure of the NBP-CNW-NTAs were investigated by SEM characterization. The results show that the use of pure [VEIM]BF_4 led to the formation of intact B and N codoped carbon NTAs (BN-CNTAs) without any porous structure in the carbon layer (Fig. S2A) due to the lack of the pore-forming agent [OMIM]PF_6. With the addition of [OMIM]PF_6 into [VEIM]BF_4 to form a mixed IL precursor, the porous structure in the carbon layer appeared after carbonization. When the volume ratio of [OMIM]PF_6 and [VEIM]BF_4 was 1:4, a well-defined loofah-like mesoporous morphology of 2D CNWs with an integrated NTAs assembled structure was obtained (Fig. S2B). However, with the increase in the volume ratio of [OMIM]PF_6 and [VEIM]BF_4 to 1:1, the 3D NTAs structure tended to collapse and form compact BNP-CNWs wrapped on CFs (Fig. S2C). Moreover, when ZnO-NRAs/CFs was coated with pure [OMIM]PF_6, only bare CFs with few and scattered carbon species on its surface was observed under the same procedure (Fig. S2D). This is because even though ILs (e.g., [OMIM]PF_6) without cross-linking groups can also produce carbonaceous material under high temperature[29], they cannot form a compact layer to coat the ZnO-NRAs template and maintain its structure when removing the template. Consequently, both cross-linkable [VEIM]BF_4 and pore-forming [OMIM]PF_6 play important roles in the formation of the 3D NBP-CNW-NTAs structure.

X-ray diffraction (XRD) patterns were used to investigate the crystallinity of NBP-CNW-NTAs (Fig. 2A). There were two major diffraction peaks located at 25.2° and 43.5°, which were assigned to the (002) and (101) diffraction planes of graphite carbon[30]. The Raman spectra of different samples are shown in Fig. 2B, which reveals two strong peaks assigned to the typical disorder band (D-band) and graphitization carbon (G-band) at approximately 1330 and 1600 cm^{-1}, respectively. The intensity ratio of the D-band and G-band (I_D/I_G) represents the structural defects in carbon materials. The I_D/I_G values for NBP-CNW-NTAs, NBP-CNWs and NB-CNTAs were 0.95, 0.93 and 0.91, respectively. Furthermore, the I_D/I_G value of NBP-CNW-NTAs was gradually enhanced from 0.87 to 0.98 as the carbonization temperature increased from 600 °C to 800 °C (Fig. S3), representing a higher degree of crystallinity of graphitic carbon formed at a higher carbonization temperature[31].

The composition of NBP-CNW-NTAs was evaluated by X-ray photoelectron spectroscopy (XPS). The XPS survey spectrum displays five main peaks assigned to O 1 s, N 1 s, C 1 s, B 1 s and P 2p (Fig. S4), confirming the successful doping of N, B and P atoms into the carbon material. The atom contents of N, B and P were calculated to be 6.8%, 0.5% and 0.13%, respectively. High-resolution XPS spectra have further offered information about the bonding types of the C, N, B and P atoms. As shown in Fig. 2C, the core-level C 1 s spectrum can be divided into four peaks located at 285.0, 286.7, 288.5, and 290.5 eV, which were attributed to C-B/C-P/C-C/C=C, C-N/C-O, C=O, and O-C-O, respectively[32]. The N 1 s spectrum revealed that the doped N atoms existed in the form of pyridinic N (398.6 eV), pyrrolic N (399.1 eV), graphitic N (400.8 eV) and N-oxides (402.1 eV)[33], as displayed in Fig. 2D. Owing to the differences in electronic configuration and electronegativity, the N atoms doped into CNWs substantially changed the electronic properties of nearby C atoms and enabled them to be active sites[34,35]. The spectrum of P showed doublet peaks located at binding energies of 133.2 eV and 134.2 eV (Fig. 2E), which were attributed to P-O and P-C bonds, respectively[36]. Compared with N atoms, P atoms with larger atomic radii are equipped with a greater electron-donating ability. Thus, P-doped carbon materials usually show better electron delocalization and a higher density of defect sites[37]. Furthermore, there were three peaks at 190.3, 191.4, and 192.5 eV in the B 1 s spectrum, corresponding to the B-C, B-N and B-O bonds, respectively (Fig. 2F)[38]. The introduction of B atoms into the carbon bulk provides electron-donating sites for charge transfer with C atoms as well[39]. In summary, the codoping of heteroatoms into carbon material generated

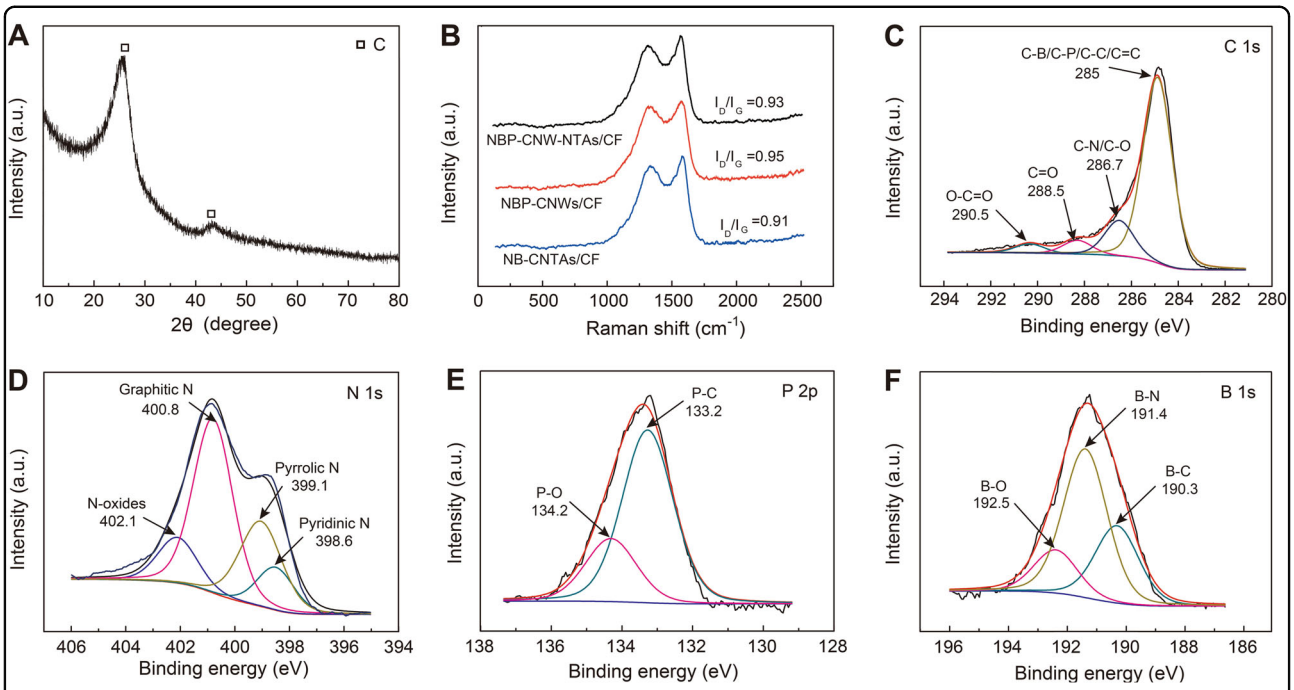

Fig. 2 The structure and composition characterization of NBP-CNW-NTAs. A XRD of NBP-CNW-NTAs. **B** Raman spectra of NBP-CNW-NTAs, NBP-CNWs and NBP-CNTAs. High-resolution XPS spectra of (**C**) C 1 s, (**D**) N 1 s, (**E**) P 2p and (**F**) B 1 s of NBP-CNW-NTAs.

synergistic effects associated with the electronic interactions between different heteroatoms and surrounding C atoms, which dramatically improved the electrocatalytic activity of the as-obtained NBP-CNW-NTAs[40].

Electrochemical sensing performances

Cyclic voltammetric (CV) measurements were performed to evaluate the electrocatalytic activity of the nanohybrid microelectrodes toward the H_2O_2 redox reaction by a standard three-electrode system with as-prepared flexible microelectrodes as WE, commercial Pt wire as CE and Ag/AgCl as RE. Figure 3A shows the CV curves of the NBP-CNW-NTAs/CF microelectrode with NBP-CNW/CF and NB-CNTAs/CF as the control in 0.1 M phosphate buffer solution (PBS) containing 8 mM H_2O_2. The CV curve of the NBP-CNW-NTAs/CF microelectrode exhibited a distinct peak at −0.25 V corresponding to the electrochemical reduction of H_2O_2, and the peak current density was much higher than that of NBP-CNW/CF and NB-CNTAs/CF. This demonstrated that NBP-CNW-NTAs on CF possessed enhanced electrocatalytic activity toward H_2O_2, which was due to their unique structure and the synergistic contributions of different elements. The unique hierarchical nanostructure of NBP-CNW-NTAs increased the surface area of the microelectrode and provided more active sites and meso-/nanopores, which favored the rapid absorption of H_2O_2 molecules and mass/charge transfer and promoted the electrocatalytic reaction rate. Moreover, the codoping of N, B and P heteroatoms into the carbon nanomaterial changed its charge density and electronic structure, further enhancing its electrochemical activity. Furthermore, the CV responses of the NBP-CNW-NTAs/CF microelectrode synthesized by carbonization at different temperatures in 0.1 M PBS containing 8 mM H_2O_2 were compared. The results showed that the H_2O_2 reduction peak current density gradually increased when the carbonizing temperature increased from 600 °C to 750 °C, which was attributed to the higher degree of crystallinity of graphitic carbon formed at a higher carbonizing temperature. However, when the carbonizing temperature reached 800 °C, the microstructure of NBP-CNW-NTAs on CF began to be destroyed, leading to a decreased peak current response (Fig. S5). Therefore, the optimal carbonizing temperature for the synthesis of NBP-CNW-NTAs/CF with a superior performance is 750 °C.

Figure 3B shows the CV curves of the NBP-CNW-NTAs/CF microelectrode in 0.1 M PBS containing different concentrations of H_2O_2, which exhibited substantially enhanced reduction peak current densities as the H_2O_2 concentrations increase from 0 mM to 10 mM, indicating that the NBP-CNW-NTAs/CF microelectrode possessed effective electrocatalytic activity for the H_2O_2 reduction reaction. At the optimum applied potential of −0.25 V, well-defined steady-state amperometric current responses were obtained within 4 s upon aliquot additions of H_2O_2, and the current densities

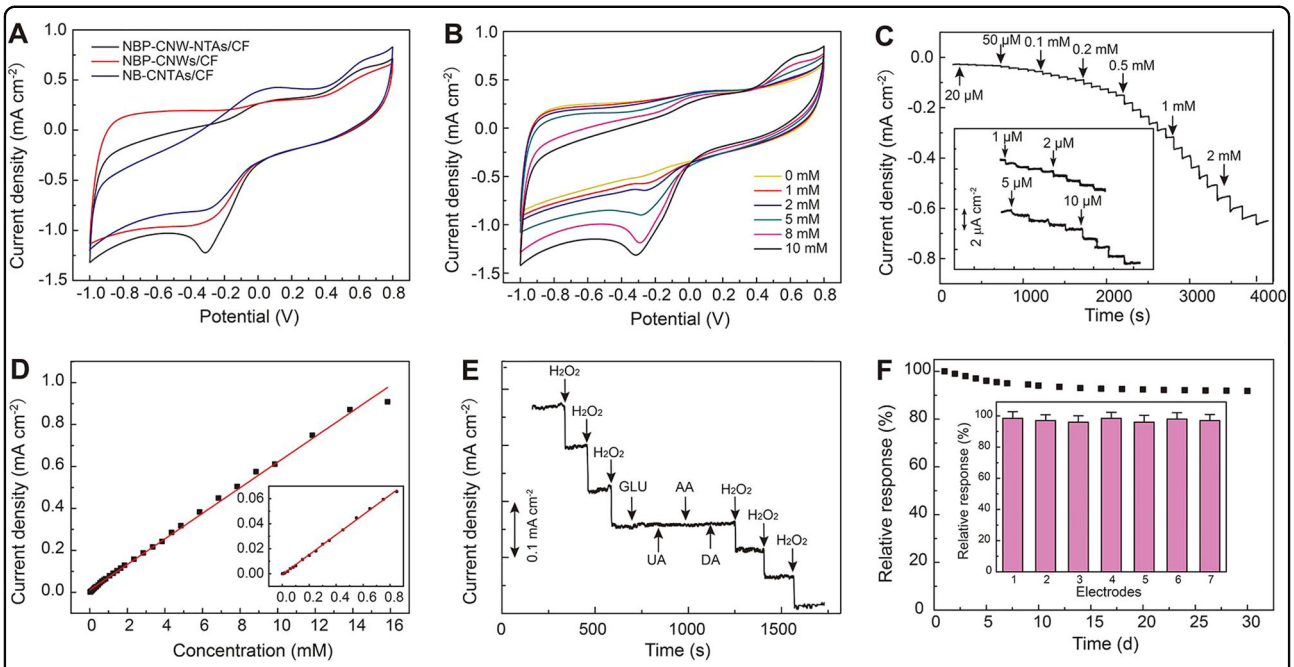

Fig. 3 The electrochemical sensing performances of NBP-CNW-NTAs/CF microelectrode toward H_2O_2. **A** CV curves of NBP-CNW-NTAs/CF, NBP-CNW/CF and NBP-CNTAs/CF microelectrodes in 0.1 M PBS solution containing 8 mM H_2O_2. Scan rate: 50 mV s^{-1}. **B** CV curves of the NBP-CNW-NTAs/CF microelectrode in 0.1 M PBS solution (pH 7.4) containing 0, 1, 2, 5, 8, and 10 mM H_2O_2. **C** Amperometric *j*-t responses of the NBP-CNW-NTAs/CF microelectrode to the addition of different H_2O_2 concentrations into 0.1 M PBS (pH 7.4) under stirring. Inset of (**C**) is the amperometric response of the NBP-CNW-NTAs/CF microelectrode to a low concentration of H_2O_2. Applied potential: −0.25 V. **D** Calibration curves of the linear relationship between the corresponding current densities and H_2O_2 concentrations. **E** Amperometric response of the NBP-CNW-NTAs/CF microelectrode to the successive addition of 0.5 mM H_2O_2 and 5.0 mM GLU, UA, AA and DA in 0.1 M PBS at −0.25 V. **F** Relative response of the NBP-CNW-NTAs/CF microelectrode to 0.5 mM H_2O_2 for 30 days. The inset is the relative response of seven different electrodes to 0.5 mM H_2O_2.

increased stepwise with the successive increase in the H_2O_2 concentration (Fig. 3C), with a linear dynamic range from 1 μM to 15.92 mM, a high sensitivity of 61.8 μA cm^{-2} mM^{-1}, and a low detection limit of 500 nM (a signal-to-noise ratio S/N = 3) (Fig. 3D). To investigate the anti-interference ability of the NBP-CNW-NTAs/CF microelectrode, several typical electroactive species, such as dopamine (DA), ascorbic acid (AA), uric acid (UA) and glucose (GLU), were injected into PBS at a concentration of 5.0 mM after adding 0.5 mM H_2O_2 three times (Fig. 3E), and there were no obvious changes in the amperometric current response of H_2O_2 in the presence of foreign interference, indicating the good anti-interference ability of the NBP-CNW-NTAs/CF microelectrode.

The long-term operation stability of the NBP-CNW-NTAs/CF microelectrode was assessed by repeatedly measuring the amperometric current responses of one electrode to 0.5 mM H_2O_2 after storage for 30 days, which revealed that the current density retained over 90% of its initial value for testing. Then, seven different NBP-CNW-NTAs/CF microelectrodes prepared by the same procedure were used to detect 0.5 mM H_2O_2, and the relative standard deviation (RSD) of the amperometric current response was calculated to be 3.9% (Fig. 3F), indicating the good reproducibility of the NBP-CNW-NTAs/CF microelectrode for practical application. Furthermore, the mechanical stability of the NBP-CNW-NTAs/CF microelectrode was also investigated with amperometric measurements. The results showed that the amperometric current responses of the microelectrode toward 0.5 mM H_2O_2 were 96.8%, 96.4%, 97.0% and 96.0% of the original value after the microelectrode was bent to 45°, 90°, 135° and 180°, respectively. In addition, the current signal only decreased ~6% when the electrode was bent to 180° by 250 times. The change in the value of the current response was 6.8%, even when the microelectrode was bent to 180° for 7 days (Fig. S6). These results demonstrated that the NBP-CNW-NTAs/CF microelectrode possessed good mechanical stability, and its electrochemical performance was almost unaffected by bending forces. The excellent mechanical properties of freestanding fiber-based microelectrodes provide a prerequisite for the development of next-generation flexible microelectrochemical sensors and integrated devices.

Real-time tracking of cancer cells by an electrochemical microfluidic biosensor

Benefiting from its exceptional electrochemical sensing performance as well as the good biocompatibility, the proposed NBP-CNW-NTAs/CF microelectrode was

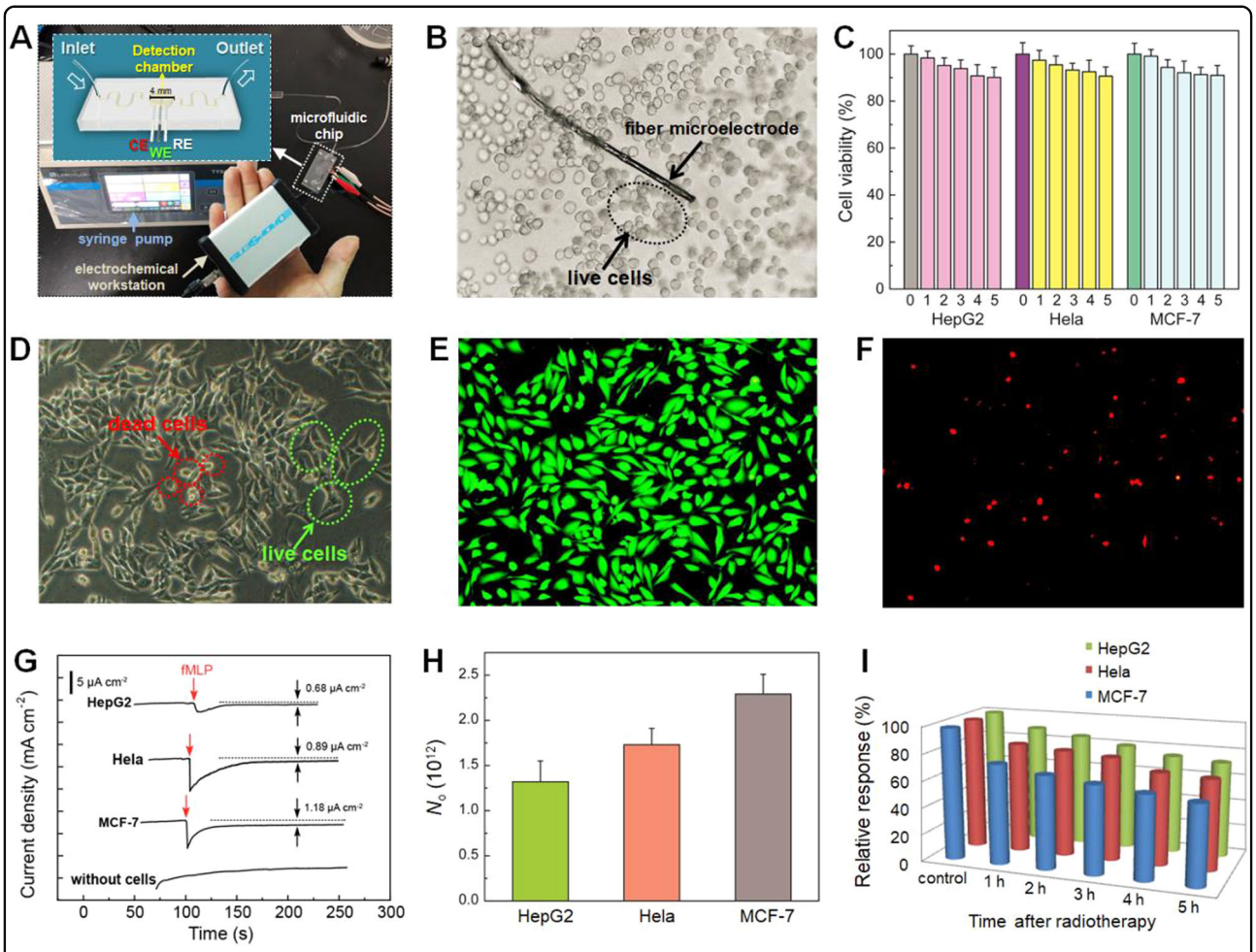

Fig. 4 Real-time tracking of cancer cells by an electrochemical microfluidic biosensor based on NBP-CNW-NTAs/CF. A Digital photo of the homemade microfluidic electrochemical sensing system. **B** Superresolution digital microscope images of MCF-7 cells incubated with NBP-CNW-NTAs/CF in the chip. **C** Quantitative cell viability results of CCK-8 assay for different cancer cells incubated with the NBP-CNW-NTAs/CF microelectrode from 0 h to 5 h. **D**–**F** Bright-field and dark-field fluorescent images of MCF-7 cells after the calcein-AM/PI assay to stain the viable cells green by calcein-AM and dead cells red by PI. **G** Amperometric current responses of the electrochemical sensor to the addition of 0.1 mM fMLP into the test solutions with HepG2, HeLa and MCF-7 cells and without cells. **H** Histograms of the N_o values for HepG2, HeLa and MCF-7 cells. **I** Histograms of the N_o values for MCF-7 cells after 0 h (control), 1, 2, 3, 4 and 5 h of radiotherapy and without any treatment.

further employed for the ultrasensitive detection of H_2O_2 in three types of live cancer cells, including hepatoma cells (i.e., HepG2), cervical cancer cells (i.e., HeLa) and breast cancer cells (i.e., MCF-7). Figure 4A shows that the freestanding flexible microelectrode was embedded in a homemade electrochemical microfluidic chip and functioned as the WE, with homemade Pt wire and Ag wire as the CE and RE, respectively. The resultant electrochemical microfluidic sensor was connected with a portable bipotentiostat to record the electrochemical signals. The cell culture solutions containing different live cells were injected into the chip and incubated with NBP-CNW-NTAs/CF to reach a high cell density of 5×10^6 cells mL^{-1} (Fig. 4B). Quantitative analysis of the standard cell counting Kit-8 (CCK-8) assay results showed that all live HepG2, HeLa and MCF-7 cells maintained more than 90% viability after incubation with NBP-CNW-NTAs/CF for 5 h (Fig. 4C). For comparison, all live cells maintained more than 93% viability after incubation in the chip in the absence of NBP-CNW-NTAs/CF for 5 h (Fig. S7). The dual-fluorescent calcein-AM/PI assay results shown in Fig. 4D and E indicated that the MCF-7 cells incubated with NBP-CNW-NTAs/CF for 5 h were quite healthy, and very few dead cells were observed in the dark-field fluorescent image (Fig. 4F). Owing to the good biocompatibility of carbon-based materials, NBP-CNW-NTAs/CF exhibited a quite low cytotoxicity to live human cells, which enabled it to be used as an implantable electrochemical probe for the in vitro and in vivo sensitive detection of different human real samples.

For the real-time in situ tracking of H_2O_2 released by live cancer cells, N-formylmethionyl-leucyl-phenylalanine (fMLP) was used as an artificial stimulator to irritate live cells to exude H_2O_2. Figure 4G shows that after the addition of 0.1 mM fMLP into each chip containing HepG2, HeLa and MCF-7 cells, the amperometric current density increased by 0.68 μA cm^{-2}, 0.89 μA cm^{-2} and 1.18 μA cm^{-2}, respectively. Under the same conditions, no obvious change was observed in the blank testing solution without cells, which indicated that the increased amperometric current responses originated from H_2O_2 released by live cells under stimulation. According to our previous works, the number of released H_2O_2 molecules per cell can be calculated by the equation $N_o = [(\Delta j/S) \times N_A)]/N_{cell}$, where Δj is the increased amperometric current density in Fig. 4H, S is the sensitivity from the calibration curve in Fig. 3D (i.e., 100.3 μA cm^{-2} mM^{-1}), N_A is the Avogadro constant (6.02×10^{23} $mole^{-1}$), and N_{cell} is the cell density (5×10^6 cells mL^{-1}). The N_o values were calculated to be 1.32×10^{12}, 1.73×10^{12}, and 2.29×10^{12} for the HepG2, HeLa and MCF-7 cells, respectively. Evidently, the level of H_2O_2 secreted by different live cells varied with the type of cancer cells under the same stimulation. Therefore, our strategy for rapidly and accurately measuring the number of extracellular H_2O_2 molecules using the NBP-CNW-NTAs/CF microelectrode opens a new avenue for differentiating the types of cancer cells for the early screening and assessment of different cancer diseases.

Furthermore, the proposed electrochemical sensing system was also used to evaluate the radiotherapeutic effect of different live cells, and in this evaluation, HepG2, HeLa and MCF-7 cells in the chip were irradiated using a 16 MV X-ray linear accelerator at a dose rate of 200 cGy/min. As shown in Fig. 4I, after 1, 2, 3, 4 and 5 h of radiotherapy treatment, the relative amperometric current responses of the electrochemical sensor toward MCF-7 cells under stimulation declined from 100% to 75.8%, 70.5%, 66.9%, 63.4% and 60.4%, respectively. This is because exposing cancer cells to an X-ray beam triggers cell death and reduces the number of viable cells, which results in decreased electrochemical responses toward the H_2O_2 secreted by live cells. However, under the same conditions, the relative responses for HeLa cells declined from 100% to 83.4% and 81.0%. 78.6%, 70.2% and 68.5% at 1, 2, 3, 4 and 5 h after radiotherapy treatment, respectively. The values for HepG2 ranged from 100% to 89.5%, 85.4%, 80.3%, 74.8% and 72.6% under the same conditions. Remarkably, radiotherapy treatment by X-ray has high therapeutic activity against all live cancer cells. MCF-7 cells are more sensitive to radiotherapy treatment than the other two types of cancer cells. This is of vital scientific significance for the rapid and effective evaluation of therapeutic efficiency in the treatment of different cancers.

In situ detection of tumor tissues by an electrochemical implantable probe

With regard to clinical practice, the freestanding flexible nanostructured microelectrode was further integrated into an implantable probe for tumor tissue detection. As shown in Fig. 5A and B, two surgically resected clinical specimens from female patients with primary breast cancer, with weights of 138 mg (denoted as tumor tissue I) and 225 mg (denoted as tumor tissue II), were selected for testing, and the corresponding histological microscopic images with H&E staining showed the live cancer cells. For comparison, adipose tissue that enclosed tumor tissue I was dissected and used as the control (weight: 142 mg, denoted as control), as shown in Fig. 5C. For the in situ detection of H_2O_2 in real human tissues, the integrated implantable probe was inserted inside different breast samples, with the flexible NBP-CNW-NTAs/CF microelectrode as the WE (Fig. 5D). Upon the addition of 0.1 mM fMLP into the testing solution containing breast tumor tissues, dramatically increased amperometric current densities were obtained. In comparison, there was no change in the amperometric response in the blank solution without tissues. This is consistent with the results of cancer cell testing, demonstrating the electrochemical responses derived from H_2O_2 released from live cells in tissue. More importantly, it was observed that under the same conditions, the increased amperometric current densities from tumor tissue I, tumor tissue II and the control tissue were 1.41 μA cm^{-2}, 1.86 μA cm^{-2} and 0.91 μA cm^{-2}, respectively (Fig. 5E). Significantly, the amperometric current density of tumor tissue I was much higher than that of the surrounding adipose tissue (control) because of the rapid propagation of cancer cells, which secrete larger amounts of H_2O_2 than normal cells (i.e., adipose cells). Furthermore, tumor tissue II with a larger size yielded a higher cell density in the testing solution than tumor tissue I, which delivered a higher amperometric current density from the H_2O_2 secreted by cancer cells upon stimulation (Fig. 5F). Consequently, the proposed electrochemical implantable sensor based on the NBP-CNW-NTAs/CF microelectrode provides a highly effective strategy for the minimally invasive detection of breast cancer in clinical practice.

Conclusions

In summary, we designed and synthesized a new type of 3D high-order hierarchically structured NBP-CNW-NTA by a facile, highly effective and well-controllable template method using task-specific ILs of [VEIM]BF_4 and [OMIM]PF_6 as the precursors. The modular nature of this approach offers new possibilities for synthesizing different carbon nanomaterials with the desired mesostructures, tunable porosities, high carbon yields and changeable doped heteroatoms by adjusting the template structure and the molecular organization of the anions and cations of the ILs. The structural merits and electrochemical properties of the

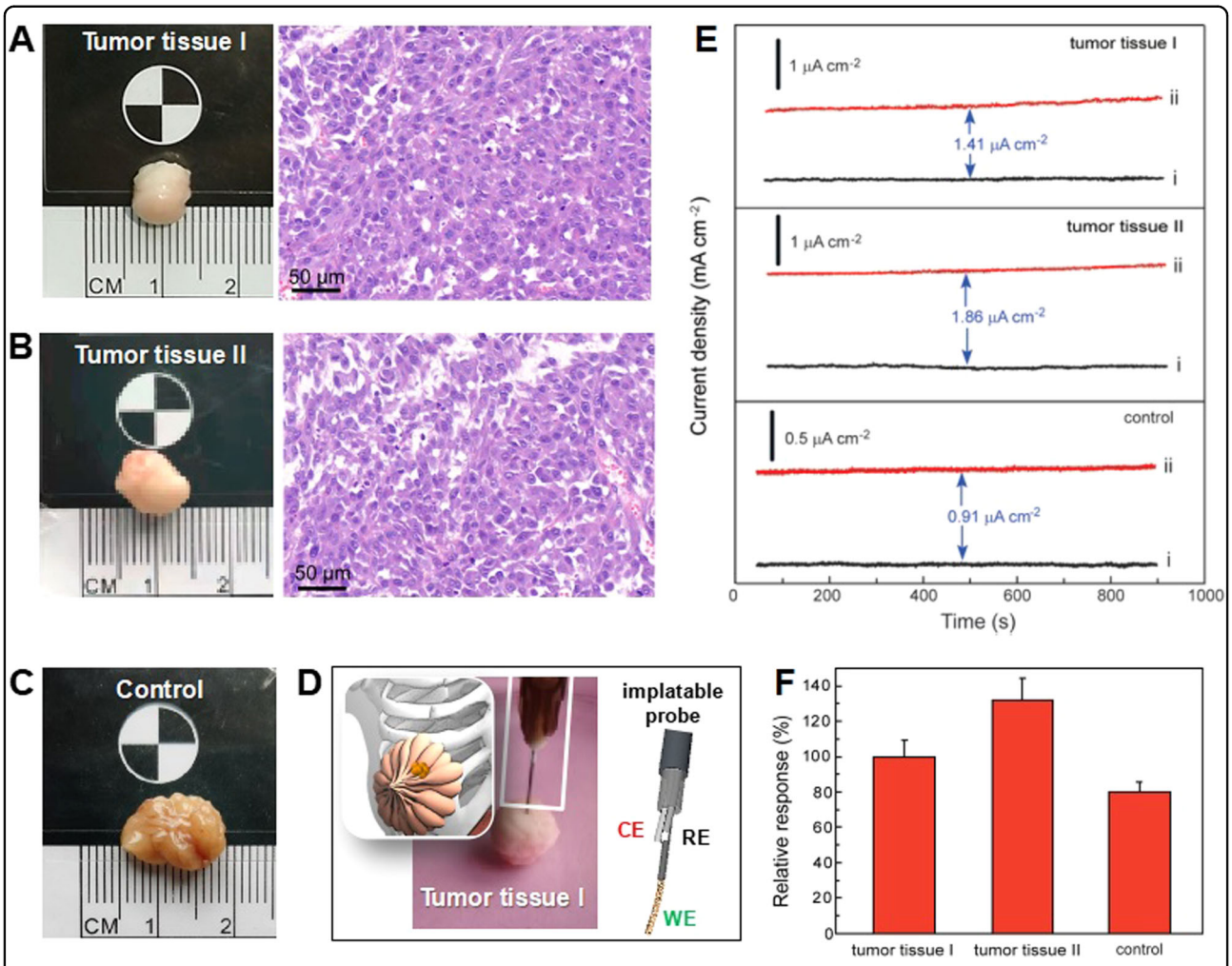

Fig. 5 In situ detection of tumor tissues by NBP-CNW-NTAs/CF based electrochemical implantable probe. A, **B** Digital photographs and histological microscopic images with H&E staining of different dissected breast tumor tissues from surgically resected clinical specimens. **C** Digital photographs of adipose tissue that enclosed tumor tissue I (control). **D** Digital photographs of the implantable probe for the in situ detection of breast tumor tissue and the scheme of the integrated probe with the flexible NBP-CNW-NTAs/CF microelectrode as the WE, Ag wire as the RE and Pt wire as the CE. **E** Amperometric current responses of the implantable probe to the addition of 0.1 mM fMLP into the test solutions containing different real human breast samples. **F** Histograms of the relative responses of the implantable probe to different real human breast samples under stimulation.

as-obtained NBP-CNW-NTAs/CF microelectrode resulted in a significant improvement in high electrocatalytic activity and durability in the redox reaction of the biomarker H_2O_2. As a result, the proposed microelectrode exhibited high sensitivity and selectivity, admirable mechanical and operational stability, and good biocompatibility, which enabled it to be embedded into a homemade microfluidic chip and integrated into an implantable probe for the real-time in situ detection of H_2O_2 secreted from different types of live cancer cells and tissues, which is of vital significance for cancer diagnosis and therapy. We envision that this strategy for the construction of high-order NBP-CNW-NTAs on flexible microelectrodes holds great promise for their extensive applications in next-generation miniaturized and implantable electrochemical devices for biosensing and biomedical engineering, as well as energy-related systems, which will contribute to the future development of functional materials, nanotechnology, electrochemistry, clinical medicine and so on.

Acknowledgements
This work is supported by the National Natural Science Foundation of China (Project No. 21874051, 51504168 and 82072944), Natural Science Foundation of Hubei Province (No. 2020CFB786), Internal Research Funding of Khalifa University of Science and Technology (KU) (CIRA-2018-16), and program for HUST Academic Frontier Youth Team (2019QYTD11). We thank the Analytical and Testing Center of Huazhong University of Science and Technology and the Wuhan National Laboratory for Optoelectronics.

Author details
[1]Hubei Key Laboratory of Plasma Chemistry and Advanced Materials, School of Materials Science and Engineering, Wuhan Institute of Technology, Wuhan 430073, P. R. China. [2]Key Laboratory of Material Chemistry for Energy

Conversion and Storage, School of Chemistry and Chemical Engineering, Huazhong University of Science & Technology, Wuhan 430074, P. R. China. [3]Technology Inspection Center of ShengLi Oil Field, Dongying 257000, P. R. China. [4]Department of Breast and Thyroid Surgery, Union Hospital, Tongji Medical College, Huazhong University of Science & Technology, Wuhan 430022, P. R. China. [5]Department of Aerospace Engineering, Khalifa University of Science and Technology, P. O. Box 127788 Abu Dhabi, United Arab Emirates

Author contributions

Y.S. and F.X. conceived the concept. Y.S., W.H., K.L., and F.X. designed the experiments. Y.S., X.D., and M.A. performed the experiments. X.D., H.H., Y.Z., K.C., and Y.X. analyzed the data, Y.S., K.L., and F.X. wrote the manuscript. All authors discussed the results and commented on the manuscript.

Conflict of interest

The authors declare no competing interests.

Publisher's note

Supplementary information The online version contains supplementary material available at https://doi.org/10.1038/s41427-022-00458-5.

Received: 30 July 2022 Revised: 3 December 2022 Accepted: 8 December 2022
Published online: 31 March 2023

References

1. Lu, J., Yeo, P. S. E. & Loh, K. P. Transforming C60 molecules into graphene quantum dots. *Nat. Nanotech.* **6**, 247–252 (2011).
2. Zhong, D. et al. Twin physically unclonable functions based on aligned carbon nanotube arrays. *Nat. Electron.* https://doi.org/10.1038/s41928-022-00787-x (in press).
3. Li, S. Y. et al. Imaging topological and correlated insulating states in twisted monolayer-bilayer graphene. *Nat. Commun.* **13**, 4225 (2022).
4. Cao, Z.-Q., Wu, M.-Z., Hu, H.-B., Liang, G.-J. & Zhi, C.-Y. Monodisperse Co_9S_8 nanoparticles in situ embedded within N, S-codoped honeycomb-structured porous carbon for bifunctional oxygen electrocatalyst in a rechargeable Zn–air battery. *NPG Asia Mater.* **10**, 670–684 (2018).
5. Xu, Y., Huang, W., Zhang, Y., Duan, H. & Xiao, F. Electrochemical microfluidic multiplexed bioanalysis by highly active bottlebrush-like nanocarbon microelectrode. *Anal. Chem.* **94**, 4463–4473 (2022).
6. Loh, K. P. et al. Clinical applications of carbon nanomaterials in diagnostics and therapy. *Adv. Mater.* **30**, 1802368 (2018).
7. Tomarchio, L. et al. Disordered photonics behavior from terahertz to ultraviolet of a three-dimensional graphene network. *NPG Asia Mater.* **13**, 73 (2021).
8. Sun, Z., Fang, S. & Hu, Y. H. 3D graphene materials: from understanding to design and synthesis control. *Chem. Rev.* **120**, 10336–10453 (2020).
9. Lee, S.-K. et al. 3D-networked carbon nanotube/diamond core-shell nanowires for enhanced electrochemical performance. *NPG Asia Mater.* **6**, e115 (2014).
10. Liu, Z. et al. Three-dimensional ordered porous electrode materials for electrochemical energy storage. *NPG Asia Mater.* **11**, 12 (2019).
11. Sun, Y. et al. Ultrasonic-electrodeposition of PtPd alloy nanoparticles on ionic liquid-functionalized graphene paper: towards a flexible and versatile nanohybrid electrode. *Nanoscale* **8**, 1523–1534 (2016).
12. Pang, K. et al. Hydroplastic foaming of graphene aerogels and artificially intelligent tactile sensors. *Sci. Adv.* **6**, eabd4045 (2020).
13. Wang, L. et al. PtAu alloy nanoflowers on 3D porous ionic liquid functionalized graphene-wrapped activated carbon fiber as a flexible microelectrode for near-cell detection of cancer. *NPG Asia Mater.* **8**, e337 (2016).
14. Xiao, F. et al. Coating graphene paper with 2D-assembly of electrocatalytic nanoparticles: a modular approach toward high-performance flexible electrodes. *ACS Nano* **6**, 100–110 (2012).
15. Zhang, Z. et al. Facile synthesis of 3D MnO_2-graphene and carbon nanotube-graphene composite networks for highperformance, flexible, all-solid-state asymmetric supercapacitors. *Adv. Energy Mater.* **4**, 1400064 (2014).
16. Yousefi, N., Lu, X., Elimelech, M. & Tufenkji, N. Environmental performance of graphene-based 3D macrostructures. *Nat. Nanotech.* **14**, 107–119 (2019).
17. Liu, J., Zhu, D., Zheng, Y., Vasileff, A. & Qiao, S. Z. Self-supported earth-abundant nanoarrays as efficient and robust electrocatalysts for energy-related reactions. *ACS Catal.* **8**, 6707–6732 (2018).
18. Zhang, Y. et al. Coral-like hierarchical structured carbon nanoscaffold with improved sensitivity for biomolecular detection in cancer tissue. *Biosens. Bioelectron.* **150**, 111924 (2022).
19. Liu, R., Mahurin, S. M., Li, C., Unocic, R. R. & Dai, S. Dopamine as a carbon source: the controlled synthesis of hollow carbon spheres and yolk-structured carbon nanocomposites. *Angew. Chem. Int. Edn.* **50**, 6799–6802 (2011).
20. Sheng, H., Wei, M., D'Aloia, A. & Wu, G. Heteroatom polymer-derived 3D high-surface-area and mesoporous graphene sheet-like carbon for supercapacitors. *ACS Appl. Mater. Inter.* **8**, 30212–30224 (2016).
21. Paraknowitsch, J. P., Zhang, J., Su, D., Thomas, A. & Antonietti, M. Ionic liquids as precursors for nitrogen-doped graphitic carbon. *Adv. Mater.* **21**, 87–92 (2013).
22. Fellinger, T. P., Thomas, A., Yuan, J. & Antonietti, M. 25th anniversary article: "cooking carbon with salt": carbon materials and carbonaceous frameworks from ionic liquids and poly(ionic liquid)s. *Adv. Mater.* **25**, 5838–5854 (2013).
23. Fulvio, P. F. et al. Boron and nitrogen-rich carbons from ionic liquid precursors with tailorable surface properties. *Phys. Chem. Chem. Phys.* **13**, 13486–13491 (2011).
24. Bedard, K. & Krause, K. H. The NOX family of ROS-generating NADPH oxidases: physiology and pathophysiology. *Physiol. Rev.* **87**, 245–313 (2007).
25. Yin, Z. M., Ivanov, V. N., Habelhah, H., Tew, K. & Ronai, Z. Glutathione S-transferase p elicits protection against H_2O_2-induced cell death via coordinated regulation of stress kinases. *Cancer Res.* **60**, 4053–4057 (2000).
26. Gao, K. et al. Efficient metal-free electrocatalysts from N-doped carbon nanomaterials: mono-doping and co-doping. *Adv. Mater.* **31**, 1805121 (2018).
27. Yuan, J. Y., Giordano, C. & Antonietti, M. Ionic liquid monomers and polymers as precursors of highly conductive, mesoporous, graphitic carbon nanostructures. *Chem. Mater.* **22**, 5003–5012 (2010).
28. Lee, J. S., Wang, X., Luo, H., Baker, G. A. & Dai, S. Facile ionothermal synthesis of microporous and mesoporous carbons from task specific ionic liquids. *J. Am. Chem. Soc.* **131**, 4596–4597 (2009).
29. Xie, Z. L. & Su, D. S. Ionic liquid based approaches to carbon materials synthesis. *Eur. J. Inorg. Chem.* **7**, 1137–1147 (2015).
30. Deng, P. et al. Conversion of biomass waste to multi-heteroatom-doped carbon networks with high surface area and hierarchical porosity for advanced supercapacitors. *J. Mater. Sci.* **53**, 14536–14547 (2018).
31. Choi, C. H., Park, S. H. & Woo, S. I. Binary and ternary doping of nitrogen, boron, and phosphorus into carbon for enhancing electrochemical oxygen reduction activity. *ACS Nano* **6**, 7084–7091 (2012).
32. Hao, R., Lan, H., Kuang, C., Wang, H. & Guo, L. Superior potassium storage in chitin-derived natural nitrogen-doped carbon nanofibers. *Carbon* **128**, 224–230 (2018).
33. lamprasertkun, P., Krittayavathananon, A. & Sawangphruk, M. N-doped reduced graphene oxide aerogel coated on carboxyl-modified carbon fiber paper for high-performance ionic-liquid supercapacitors. *Carbon* **102**, 455–461 (2016).
34. Dai, L., Xue, Y., Qu, L., Choi, H.-J. & Baek, J.-B. Metal-free catalysts for oxygen reduction reaction. *Chem. Rev.* **115**, 4823–4892 (2015).
35. Guo, D. et al. Active sites of nitrogen-doped carbon materials for oxygen reduction reaction clarified using model catalysts. *Science* **351**, 361–365 (2016).
36. Li, R., Wei, Z., Gou, X. & Xu, W. Phosphorus-doped graphene nanosheets as efficient metal-free oxygen reduction electrocatalysts. *RSC Adv.* **3**, 9978–9984 (2013).
37. Yang, D. S., Bhattacharjya, D., Inamdar, S., Park, J. & Yu, J. S. Phosphorus-doped ordered mesoporous carbons with different lengths as efficient metal-free electrocatalysts for oxygen reduction reaction in alkaline media. *J. Am. Chem. Soc.* **134**, 16127–16130 (2012).
38. Hao, J. et al. B/N co-doped carbon nanosphere frameworks as high-performance electrodes for supercapacitors. *J. Mater. Chem. A* **6**, 8053–8058 (2018).
39. Yang, L. et al. Boron-doped carbon nanotubes as metal-free electrocatalysts for the oxygen reduction reaction. *Angew. Chem. Int. Ed.* **50**, 7132–7135 (2011).
40. Liu, X. & Dai, L. Carbon-based metal-free catalysts. *Nat. Rev. Mater.* **1**, 16064 (2016).